The Computer Journal Advance Access published June 11, 2008

doi:10.1093/comjnl/bxn031

Super-Resolution of Multispectral Images

M. VEGA[1,*], J. MATEOS[2], R. MOLINA[2] AND A.K. KATSAGGELOS[3]

[1]*Departamento de Lenguajes y Sistemas Informáticos, Universidad de Granada, 18071 Granada, Spain*
[2]*Departamento de Ciencias de la Computación e I. A., Universidad de Granada, 18071 Granada, Spain*
[3]*Department of Electrical Engineering and Computer Science, Northwestern University, Evanston, IL 60208-3118, USA*
**Corresponding author: mvega@ugr.es*

In this paper we propose and analyze a globally and locally adaptive super-resolution Bayesian methodology for pansharpening of multispectral images. The methodology incorporates prior knowledge on the expected characteristics of the multispectral images uses the sensor characteristics to model the observation process of both panchromatic and multispectral images and includes information on the unknown parameters in the model in the form of hyperprior distributions. Using real and synthetic data, the pansharpened multispectral images are compared with the images obtained by other pansharpening methods and their quality is assessed both qualitatively and quantitatively.

Keywords: super-resolution; Bayesian models; hyperspectral images

Received 16 October 2007; revised 6 March 2008

1. INTRODUCTION

Nowadays most remote sensing systems include sensors able to capture, simultaneously, several low-resolution images of the same area on different wavelengths, forming a multispectral image, along with a high-resolution panchromatic image. The main characteristics of such remote sensing systems are the number of bands of the multispectral image and the resolution of those bands and the panchromatic image. The main advantage of multispectral image is that it allows for a better land type and use recognition but, due to its lower resolution, information on the objects' shape and texture may be lost. On the other hand, the panchromatic image allows for a better recognition of the objects in the image and their textures but provides no information about their spectral properties.

The objective, therefore, is to perform *multispectral image reconstruction*, that is, to jointly process the multispectral and panchromatic images in order to obtain a new multispectral image that, ideally, will exhibit the spectral characteristics of the observed multispectral images and the resolution and quality of the panchromatic image. Such an approach, also named pansharpening, will allow us, for example in the case of Landsat 7 ETM+ [1] which has a resolution of 30 m per pixel for the multispectral image and 15 m per pixel for the panchromatic one, to obtain a multispectral image with a resolution of 15 m per pixel.

A few approximations to multispectral image reconstruction have been proposed in the literature (see [2–7] for instance). Recently a few super-resolution based methods have also been proposed. Eismann and Hardie [8] proposed a *maximum a posteriori* approach that makes use of a stochastic mixing model of the underlying spectral scene content to achieve resolution enhancement beyond the intensity component of the hyperspectral image. Akgun *et al.* [9] proposed a projection onto convex sets-based algorithm to reconstruct hyperspectral images, where the hyperspectral observations from different wavelengths are represented as weighted linear combinations of a small number of basis image planes.

In this paper we follow the hierarchical Bayesian approach to obtain a solution to the super-resolution reconstruction of multispectral images problem and discuss the utilization of global and spatially varying image models. This approach provides a suitable framework for formulating the problem, as well as for modeling the characteristics of the solution and incorporating information on the set of parameters required by those models. Then, applying variational methods to approximate probability distributions, we estimate the unknown parameters and the high-resolution multispectral image.

The paper is organized as follows. In Section 2 the Bayesian modeling and inference for the super-resolution reconstruction of multispectral images are presented. The required

probability distributions for the Bayesian modeling of the super-resolution problem are formulated in Section 3. The Bayesian analysis and posterior probability approximation to obtain the parameters and the super resolved image are performed in Section 4. Experimental results on synthetic color images and real Landsat 7 ETM+ images are described in Section 5 and, finally, Section 6 concludes the paper.

2. BAYESIAN PROBLEM FORMULATION

Let us assume that $\mathbf{y}$, the multispectral image we would observe under ideal conditions with a high-resolution sensor, has B bands $\mathbf{y}_b$, $b = 1, \ldots, B$, that is, $\mathbf{y} = [\mathbf{y}_1^t, \mathbf{y}_2^t, \ldots, \mathbf{y}_B^t]^t$, where each band is of size $p = m \times n$ pixels and the superscript t denotes the transpose of a vector or matrix. Each band of this image is expressed as a column vector by lexicographically ordering its pixels. In real applications, this high-resolution image is not available. Instead, we observe a low-resolution multispectral image $\mathbf{Y}$ with B bands $\mathbf{Y}_b$, $b = 1, \ldots, B$, that is, $\mathbf{Y} = [\mathbf{Y}_1^t, \mathbf{Y}_2^t, \ldots, \mathbf{Y}_B^t]^t$, where each band is of size $P = M \times N$ pixels with $M < m$ and $N > n$. Each band of this image is also expressed as a column vector by lexicographically ordering its pixels. The sensor also provides us with a panchromatic image $\mathbf{x}$ of size $p = m \times n$, obtained by spectrally averaging the unknown high-resolution images $\mathbf{y}_b$.

The objective of the high-resolution multispectral image reconstruction problem is to obtain an estimate of the unknown high-resolution multispectral image $\mathbf{y}$ given the panchromatic high-resolution observation $\mathbf{x}$ and the low-resolution multispectral observation $\mathbf{Y}$.

Using the hierarchical Bayesian paradigm (see [10], for example) the following joint distribution for $\mathbf{\Omega}_M$, $\mathbf{y}$, $\mathbf{Y}$ and $\mathbf{x}$ is defined $\mathrm{p}(\mathbf{\Omega}_M, \mathbf{y}, \mathbf{Y}, \mathbf{x}) = \mathrm{p}(\mathbf{\Omega}_M)\,\mathrm{p}(\mathbf{y}|\Omega_M)\,\mathrm{p}(\mathbf{Y}, \mathbf{x}|\mathbf{y}, \mathbf{\Omega}_M)$, where $\mathbf{\Omega}_M$ denotes the set of hyperparameters needed by these probability density functions, as described next (obviously, depending on the probability models used in the problem, the set of hyperparameters will differ).

The Bayesian paradigm dictates that inference on the unknowns $(\mathbf{\Omega}_M, \mathbf{y})$ should be based on $\mathrm{p}(\mathbf{\Omega}_M, \mathbf{y}|\mathbf{Y}, \mathbf{x}) = \mathrm{p}(\mathbf{\Omega}_M, \mathbf{y}, \mathbf{Y}, \mathbf{x}) / \mathrm{p}(\mathbf{Y}, \mathbf{x})$.

3. BAYESIAN MODELING

We assume that $\mathbf{Y}$ and $\mathbf{x}$, for a given $\mathbf{y}$ and a set of parameters $\mathbf{\Omega}_M$, are independent and consequently write $\mathrm{p}(\mathbf{Y}, \mathbf{x}|\mathbf{y}, \mathbf{\Omega}_M) = \mathrm{p}(\mathbf{Y}|\mathbf{y}, \mathbf{\Omega}_M)\,\mathrm{p}(\mathbf{x}|\mathbf{y}, \mathbf{\Omega}_M)$.

Each low-resolution band, $\mathbf{Y}_b$, is related to its corresponding high-resolution image by

$$\mathbf{Y}_b = \mathbf{DH}\mathbf{y}_b + \mathbf{n}_b, \quad \forall b = 1, \ldots, B, \tag{1}$$

where $\mathbf{H}$ is a $p \times p$ blurring matrix, $\mathbf{D}$ is a $P \times p$ decimation operator, and $\mathbf{n}_b$ is the capture noise, assumed to be Gaussian with zero mean and variance $1/\beta_b$.

Given the degradation model of Equation (1) and assuming independence among the noises observed in the low-resolution images, the distribution of the observed $\mathbf{Y}$ given $\mathbf{y}$ and a set of parameters $\mathbf{\Omega}_M$ is

$$\begin{aligned} \mathrm{p}(\mathbf{Y}\,|\,\mathbf{y}, \mathbf{\Omega}_M) &= \prod_{b=1}^{B} \mathrm{p}(\mathbf{Y}_b\,|\,\mathbf{y}_b, \beta_b) \\ &\propto \prod_{b=1}^{B} \beta_b^{P/2} \exp\left\{-\frac{1}{2}\beta_b \|\mathbf{Y}_b - \mathbf{DH}\mathbf{y}_b\|^2\right\}. \end{aligned} \tag{2}$$

Note that this noise model is being used widely in the literature for multispectral image super-resolution. For applications for which an independent Poisson noise model within each band is applicable, Equation (2) has to be rewritten and the approach in [11] has to be modified to deal with the super-resolution of multispectral images under this observation model.

As already mentioned, the panchromatic image $\mathbf{x}$ is obtained by spectral averaging the unknown high-resolution images $\mathbf{y}_b$, modeled as

$$\mathbf{x} = \sum_{b=1}^{B} \lambda_b \mathbf{y}_b + \mathbf{v}, \tag{3}$$

where $\lambda_b \geq 0$, $b = 1, 2, \ldots, B$ are known quantities that can be obtained, as we will see later, from the sensor spectral characteristics, and $\mathbf{v}$ is the capture noise that is assumed to be Gaussian with zero mean and variance γ^{-1}. Note that, usually, $\mathbf{x}$ does not depend on all the multispectral image bands but on a subset of them, i. e. some of the λ_bs are equal to zero.

Using the degradation model in Equation (3), the distribution of the panchromatic image $\mathbf{x}$ given $\mathbf{y}$, and a set of parameters $\mathbf{\Omega}_M$ is given by

$$\mathrm{p}(\mathbf{x}\mid \mathbf{y}, \mathbf{\Omega}_M) \propto \gamma^{p/2} \exp\left\{-\frac{1}{2}\gamma \|\,\mathbf{x} - \sum_{b=1}^{B} \lambda_b \mathbf{y}_b\,\|^2\right\}. \tag{4}$$

From the above definition, the parameter vector $(\gamma, \beta_1, \ldots, \beta_B)$ is a subset of $\mathbf{\Omega}_M$. However, although the estimation of $(\gamma, \beta_1, \ldots, \beta_B)$ can be easily incorporated into the estimation process, we will assume here that these parameters have been estimated in advance and concentrate on gaining insight into the distribution of the prior image parameters, as described next.

3.1. Global and local image modeling

In this paper we present a global image model, which enforces the same similarity among all pixels in each image band, and a

local image model that allows local variations at a pixel level in each band.

For the global image model, we assume a conditional auto-regressive (*CAR*) model [12], that is, (we use $M = G$ to denote it)

$$\mathrm{p}(\mathbf{y} \mid \mathbf{\Omega}_G) \propto \prod_{b=1}^{B} \bar{\alpha}_b^{p/2} \exp\left\{-\frac{1}{2}\bar{\alpha}_b \left[\mathbf{y}_b^{\mathrm{t}} \mathbf{C} \mathbf{y}_b\right]\right\}, \tag{5}$$

where $\mathbf{C}$ is a Laplacian operator involving the eight nearest neighbors of each pixel as shown in Fig. 1. The set of hyperparameters involved using this model are, then,

$$\mathbf{\Omega}_G = (\bar{\alpha}_1, \ldots, \bar{\alpha}_B). \tag{6}$$

Although the model in Equation (5) works well in regions where pixels have similar values (flat areas), it fails to capture the boundaries of objects and oversmoothes highly textured objects. Hence, we define a local model for the high-resolution multispectral image ($M = L$ will be used to denote it) which captures the local properties of the image, such as edges and textures, by defining a different smoothness parameter for each pixel and each direction.

For its definition we use the notation $i1, i2, \ldots, i8$ to denote the eight pixels around pixel i (see Fig. 1). Then, following the approximation in Ref. [13], which extends conditional auto-regressions to take into account local variability, we write (see Ref. [14])

$$\mathrm{p}(\mathbf{y} \mid \mathbf{\Omega}_L) = \prod_{b=1}^{B} \mathrm{p}(\mathbf{y}_b \mid \boldsymbol{\alpha}_b) \propto \prod_{b=1}^{B} \prod_{i=1}^{p} \prod_{l=1}^{4} \alpha_b(i, il)^{1/8} \exp\left\{-\frac{1}{16}\alpha_b(i, il)\left[y_b(i) - y_b(il)\right]^2\right\}, \tag{7}$$

where $\alpha_b(i,\ il)$ controls the smoothness of the reconstruction between pixels i and il for the b-band and $\boldsymbol{\alpha}_b = (\alpha_b(i,\ il) \mid i = 1, \ldots, p,\ l = 1, \ldots, 4)$. Note that if $\alpha_b(i,\ il) = \bar{\alpha}_b,\ \forall i = 1, \ldots, p,\ l = 1, \ldots, 4$, the local image model becomes the global model previously defined.

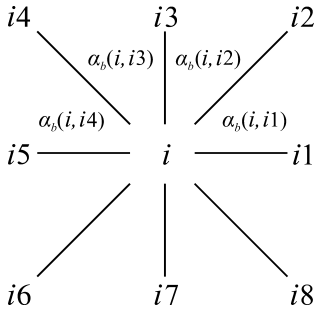

FIGURE 1. Local image model hyperparameters.

The set of hyperparameters now becomes

$$\mathbf{\Omega}_L = (\boldsymbol{\alpha}_1, \ldots, \boldsymbol{\alpha}_B). \tag{8}$$

In situations when no prior information about the hyperparameters $\Omega_M\,(M \in \{G,L\})$ exists, we can use non-informative prior on them (the term 'non-informative' is meant to imply that no information about the hyperparameters is contained in the priors). In this case, improper non-informative priors $\mathrm{p}(\mathbf{\Omega}_M) \propto$ const over $[0, \infty)$ can be used. However, it is also possible, as we shall see now, to incorporate precise prior knowledge about the value of the hyperparameters. Let us examine the hyperpriors we shall use.

In general, depending on the hyperpriors $\mathrm{p}(\mathbf{\Omega}_M)$, $\mathrm{M} \in \{G,\ L\}$, used, $\mathrm{p}(\mathbf{\Omega}_M, \mathbf{y}|\mathbf{x}, \mathbf{Y})$ may not be easily computable. A large part of the Bayesian literature is devoted to finding hyperprior distributions $\mathrm{p}(\mathbf{\Omega}_M)$, $M \in \{G,\ L\}$, for which $\mathrm{p}(\mathbf{\Omega}_M, \mathbf{y}|\mathbf{x}, \mathbf{Y})$ can be calculated in a straightforward way or can be approximated. These are the so-called conjugate priors [15] that, as we will see later, have the intuitive feature of allowing one to begin with a certain functional form for the prior and end up with a posterior of the same functional form, but with the parameters updated by the sample information.

Taking the above considerations about conjugate priors into account, we use, for both the global and local models, as hyperpriors gamma distributions. They represent conjugate priors which will allow us to incorporate into the reconstruction process precise prior knowledge about the expected value of the parameters and, also, about the confidence on such expected value.

That is, for the hyperparameters of the global model we use the distribution

$$\mathrm{p}(\mathbf{\Omega}_G) = \prod_{b=1}^{B} \mathrm{p}(\bar{\alpha}_b \mid \bar{a}_b^o, \bar{c}_b^o), \tag{9}$$

$\bar{c}_b^o > 0$ and $\bar{a}_b^o > 0$, while, for the local model, we use

$$\mathrm{p}(\mathbf{\Omega}_L) = \prod_{b=1}^{B} \prod_{i=1}^{p} \prod_{l=1}^{4} \mathrm{p}(\alpha_b(i, il) \mid a_b^o, c_b^o), \tag{10}$$

where $c_b^o > 0$ and $a_b^o > 0$ (note that the same hyperprior is assumed for all the αs in the same band).

The gamma distribution has the form

$$\mathrm{p}(\omega \mid u, v) \propto \omega^{u-1} \exp[-v\omega], \tag{11}$$

where $\omega > 0$, $u > 0$ and $v > 0$ with mean and variance

$$\mathbf{E}[\omega] = \frac{u}{v}, \quad \mathbf{var}[\omega] = \frac{u}{v^2} \tag{12}$$

(u and v are referred to as scale and precision parameters, respectively).

Finally, combining the first and second stage of the problem modeling we have the global distribution

$$\mathrm{p}(\mathbf{\Omega}_M, \mathbf{y}, \mathbf{Y}, \mathbf{x}) = \mathrm{p}(\mathbf{\Omega}_M)\,\mathrm{p}(\mathbf{y}\,|\,\mathbf{\Omega}_M)\,\mathrm{p}(\mathbf{Y}\,|\,\mathbf{y})\,\mathrm{p}(\mathbf{x}\,|\,\mathbf{y}), \tag{13}$$

for $M \in \{G, L\}$.

4. BAYESIAN INFERENCE AND VARIATIONAL APPROXIMATION OF THE POSTERIOR DISTRIBUTION

For our selection of hyperparameters in the previous section, the set of all unknowns is ($\mathbf{\Omega}_M$, $\mathbf{y}$). As already explained, the Bayesian paradigm dictates that inference on ($\mathbf{\Omega}_M$, $\mathbf{y}$) should be based on $\mathrm{p}(\mathbf{\Omega}_M, \mathbf{y}|\mathbf{Y}, \mathbf{x})$.

Since $\mathrm{p}(\mathbf{\Omega}_M, \mathbf{y}|\mathbf{Y}, \mathbf{x})$ cannot be found in closed form, because $\mathrm{p}(\mathbf{Y}, \mathbf{x})$ cannot be calculated analytically, we apply variational methods to approximate this distribution by the distribution $\mathrm{q}(\mathbf{\Omega}_M, \mathbf{y})$.

The variational criterion used to find $\mathrm{q}(\mathbf{\Omega}_M, \mathbf{y})$ is the minimization of the Kullback–Leibler (KL) divergence, given by [16, 17]

$$\begin{aligned} &C_{\mathrm{KL}}(\mathrm{q}(\mathbf{\Omega}_M, \mathbf{y}) \| \,\mathrm{p}(\mathbf{\Omega}_M, \mathbf{y}\,|\,\mathbf{Y}, \mathbf{x})) \\ &\quad = \int \mathrm{q}(\mathbf{\Omega}_M, \mathbf{y}) \log\left(\frac{\mathrm{q}(\mathbf{\Omega}_M, \mathbf{y})}{\mathrm{p}(\mathbf{\Omega}_M, \mathbf{y}\,|\,\mathbf{Y}, \mathbf{x})}\right) \mathrm{d}\Omega_M\,\mathrm{d}\mathbf{y} \\ &\quad = \int \mathrm{q}(\mathbf{\Omega}_M, \mathbf{y}) \log\left(\frac{\mathrm{q}(\mathbf{\Omega}_M, \mathbf{y})}{\mathrm{p}(\mathbf{\Omega}_M, \mathbf{y}, \mathbf{Y}, \mathbf{x})}\right) \mathrm{d}\mathbf{\Omega}_M\,\mathrm{d}\mathbf{y} + \text{const}, \end{aligned} \tag{14}$$

which is always non-negative and equal to zero only when $\mathrm{q}(\mathbf{\Omega}_M, \mathbf{y}) = \mathrm{p}(\mathbf{\Omega}_M, \mathbf{y}|\mathbf{Y}, \mathbf{x})$.

We choose to approximate the posterior distribution $\mathrm{p}(\mathbf{\Omega}_M, \mathbf{y}|\mathbf{Y}, \mathbf{x})$ by the distribution

$$\mathrm{q}(\mathbf{\Omega}_M, \mathbf{y}) = \mathrm{q}(\mathbf{\Omega}_M)\mathrm{q}_D(\mathbf{y}), \tag{15}$$

where $\mathrm{q}(\mathbf{\Omega}_M)$ denotes a distribution on $\mathbf{\Omega}_M$ and $\mathrm{q}_D(\mathbf{y})$ denotes a degenerate distribution on $\mathbf{y}$.

Note that other distribution approximations are also possible. However, as we will see later the one used here alleviates the problem of having to estimate an enormous amount of hyperparameters. We now proceed to find the best of these distributions in the divergence sense. Let us assume that $\mathbf{y}^k$ is the current estimate of the multispectral image where $\mathrm{q}_D(\mathbf{y})$ is degenerate.

Given $\mathrm{q}_D^k(\mathbf{y})$, the current estimate of $\mathrm{q}_D(\mathbf{y})$, we can obtain an estimate of $\mathrm{q}(\mathbf{\Omega})$ which reduces the KL-divergence by solving

$$\begin{aligned} &\mathrm{q}^{k+1}(\mathbf{\Omega}_M) = \\ &\quad \arg \min_{\mathrm{q}(\mathbf{\Omega}_M)} C_{\mathrm{KL}}(\mathrm{q}(\mathbf{\Omega}_M), \mathrm{q}_D^k(\mathbf{y}) \| \,\mathrm{p}(\mathbf{\Omega}_M, \mathbf{y}\,|\,\mathbf{Y}, \mathbf{x})). \end{aligned} \tag{16}$$

Differentiating the integral on the right-hand side of Equation (16) with respect to $\mathrm{q}(\mathbf{\Omega}_M)$ and setting it equal to zero we obtain that for the global image model ($M = G$) in Equation (9), $\mathrm{q}^{k+1}(\mathbf{\Omega}_G)$ satisfies

$$\mathrm{q}^{k+1}(\mathbf{\Omega}_G) = \prod_{b=1}^{B} \mathrm{q}^{k+1}(\bar{\alpha}_b)\,, \tag{17}$$

where

$$\mathrm{q}^{k+1}(\bar{\alpha}_b) = \mathrm{p}\left(\bar{\alpha}_b \mid \bar{a}_b^o + \frac{p}{2}, \bar{c}_b^o + \frac{1}{2}\left[\mathbf{y}_b^{k\prime}\mathbf{C}\mathbf{y}_b^k\right]\right). \tag{18}$$

These distributions have means

$$\mathbf{E}[\bar{\alpha}_b]_{q^{k+1}(\mathbf{\Omega}_G)} = \frac{\bar{a}_b^o + (p/2)}{\bar{c}_b^o + (1/2)\left[\mathbf{y}_b^{k\prime}\mathbf{C}\mathbf{y}_b^k\right]}, \tag{19}$$

$b = 1, \ldots, B$, which can be rewritten as

$$\frac{1}{\mathbf{E}[\bar{\alpha}_b]_{q^{k+1}(\mathbf{\Omega}_\mathbf{G})}} = \bar{\mu}_b \frac{\bar{c}_b^o}{\bar{a}_b^o} + (1 - \bar{\mu}_b)\frac{\mathbf{y}_b^{k\prime}\mathbf{C}\mathbf{y}_b^k}{p}, \tag{20}$$

with

$$\bar{\mu}_b = \frac{\bar{a}_b^o}{p/2 + \bar{a}_b^o}\,, \quad b = 1, \ldots, B. \tag{21}$$

Equations (20) and (21) indicate that, for each hyperparameter of the global model, the inverse of the mean of its posterior distribution approximation is a convex combination of the inverse of the mean of its hyperprior distribution [see Equation (12)] and its maximum likelihood estimate. Furthermore, $\bar{\mu}_b$, $b = 1, \ldots, B$, can be understood as a normalized confidence parameter taking values in the interval [0, 1). That is, when it is zero no confidence is placed on the given hyperparameters, while when the corresponding normalized confidence parameter is asymptotically equal to one it fully enforces the prior knowledge on the mean (no estimation of the hyperparameters is performed).

For the local image model, that is, for $M = L$, we have

$$q^{k+1}(\mathbf{\Omega}_L) = \prod_{b=1}^{B}\prod_{i=1}^{p}\prod_{l=1}^{4} q^{k+1}(\alpha_b(i, il)), \tag{22}$$

where

$$q^{k+1}(\alpha_b(i, il)) = p\left(\alpha_b(i, il) \mid a_b^o + \frac{1}{8}, \frac{1}{16}\left[y_b^k(i) - y_b^k(il)\right]^2 + c_b^o\right). \tag{23}$$

These distributions have means

$$\mathbf{E}[\alpha_b(i, il)]_{q^{k+1}(\mathbf{\Omega}_L)} = \frac{a_b^o + (1/8)}{c_b^o + 1/16\,[y_b^k(i) - y_b^k(il)]^2}. \tag{24}$$

Note that Equation (24) can be rewritten as

$$\frac{1}{\mathbf{E}[\alpha_b(i, il)]_{q^{k+1}(\mathbf{\Omega}_L)}} = \mu_b \frac{c_b^o}{a_b^o} + (1 - \mu_b)\frac{1}{2}\left[y_b^k(i) - y_b^k(il)\right]^2, \tag{25}$$

where

$$\mu_b = \frac{a_b^o}{a_b^o + (1/8)}. \tag{26}$$

Again, as for the global model, Equations (25) and (26) indicate that μ_b can be understood as a normalized confidence parameter taking values in the interval [0, 1).

Given now $q^{k+1}(\mathbf{\Omega}_M)$ we can obtain an estimate of $\mathbf{y}^{k+1}$ (the value where $q_D^{k+1}(\mathbf{y})$ is degenerate, which obviously will depend on the image model used) that reduces the KL-divergence by solving

$$\mathbf{y}^{k+1} = \arg\min_{\mathbf{y}}\left\{-\mathbf{E}[\log\, p(\mathbf{\Omega}_M, \mathbf{y}, \mathbf{Y}, \mathbf{x})]_{q^{k+1}(\mathbf{\Omega}_M)}\right\}. \tag{27}$$

The convergence of the parameters defining the distributions $q^{k+1}(\mathbf{\Omega}_M)$ and $\mathbf{y}^{k+1}$ can be used as a stopping criterion for the proposed iterative procedure consisting of Equations (20), (25) and (27).

Let us now study the asymptotic behavior of the variance of the distribution in Equation (18). We have that for varying $\bar{\mu}_b$ with $\bar{c}_b^o/\bar{a}_b^o$ constant

$$\mathbf{var}[\bar{\alpha}_b]_{q^{k+1}(\mathbf{\Omega}_G)} \longrightarrow 0, \quad \text{for } \bar{\mu}_b \longrightarrow 1,$$
$$\mathbf{var}[\bar{\alpha}_b]_{q^{k+1}(\mathbf{\Omega}_G)} \longrightarrow \infty, \quad \text{for } \bar{\mu}_b \longrightarrow 0.$$

Similarly, for the variance of the distribution in Equation (22), we have that for varying μ_b with c_b^o/a_b^o constant

$$\mathbf{var}[\alpha_b(i, il)]_{q^{k+1}(\mathbf{\Omega}_L)} \longrightarrow 0, \quad \text{for } \mu_b \longrightarrow 1,$$
$$\mathbf{var}[\alpha_b(i, il)]_{q^{k+1}(\mathbf{\Omega}_L)} \longrightarrow \infty, \quad \text{for } \mu_b \longrightarrow 0.$$

Based on the above expression, the hyperprior distributions tend to the uniform distribution as the confidence parameters approach 0, and tend to a degenerate distribution when they approach 1. That is, the local image model becomes global when μ_b approaches 1.

5. EXPERIMENTAL RESULTS

In the preceding sections a variational method for the estimation of the posterior distribution $p(\mathbf{\Omega}_M, \mathbf{y}|\mathbf{Y}, \mathbf{x})$ has been described. Let us now study the results obtained by the proposed multispectral image reconstruction algorithm utilizing both the global ($M = G$) and local ($M = L$) image models.

In this paper the values of the parameters $\gamma, \beta_1, \ldots, \beta_B$ are first estimated using the variational approximation method described in [12] for the CAR global image model described in Equation (5). This method utilizes the following initial estimates of the hyperparameters $\gamma, \beta_1, \ldots, \beta_B$ and $\alpha_1, \ldots, \alpha_B$, based on the observed multispectral and panchromatic images, $\alpha_b = p/\mathbf{x}^t\mathbf{C}\mathbf{x}$, $\beta_b = P/\ \|\ \mathbf{Y}_b - \mathbf{DHx}\ \|^2$, for all $b = 1, \ldots, B$, and $\gamma = P\,/\,(4\ \|\ \mathbf{DHx} - \sum_{b=1}^{B}\lambda_b\mathbf{Y}_b\ \|^2)$. Using these initial parameters, the iterative procedure in [12] is used with a flat hyperprior on the hyperparameters to obtain an estimate of the precision parameters of the low-resolution and panchromatic observation models, as well as, the global prior model. The method in [12] also provides a reconstructed multispectral image that will be used as initial estimate in our iterative procedure.

The scale and precision hyperparameters of the gamma hyperpriors, $\bar{a}_b^o$ and $\bar{c}_b^o$, for $b = 1, \ldots, B$, if $M = G$, and a_b^o and c_b^o, for $b = 1, \ldots, B$, if $M = L$, have to be selected. Note that knowing the scale and precision hyperparameters is equivalent to knowing the inverse of the means of the hyperprior distributions, $\bar{c}_b^o/\bar{a}_b^o$ and c_b^o/a_b^o, together with the normalized confidence parameters $\bar{\mu}_b$ and μ_b, $b = 1, \ldots, B$, for the global and local image models, respectively.

As we have already mentioned, the super-resolution method in [12] provides us with an estimate of the inverse of the mean of the hyperprior distribution, denoted as $\underline{\alpha}_b$, for $b = 1, \ldots, B$. This value is used as an approximation of the value of the hyperparameters of the global and local image models using the following procedure. We rewrite the inverse of the mean of the hyperprior distribution on the global and local image

hyperparameter models as

$$\frac{\bar{c}_b^o}{\bar{a}_b^o} = \bar{\rho}_b \frac{1}{\underline{\alpha}_b}, \quad \text{for } b = 1, \ldots, B, \tag{28}$$

and

$$\frac{c_b^o}{a_b^o} = \rho_b \frac{1}{\underline{\alpha}_b}, \quad \text{for } b = 1, \ldots, B, \tag{29}$$

respectively.

Hence, given the estimation of the prior model hyperparameters obtained by the method in [12], the parameters we need to select are $\bar{\mu}_b$ and $\bar{\rho}_b$ for the global image model and μ_b and ρ_b for the local image model.

Our first experiment focuses on understanding the behavior of the global and local models under controlled conditions. To this end, synthetic hyperspectral and panchromatic observations have been obtained from the color images displayed in Fig. 2 degrading them according to the model in Equation (2). The original images were convolved with mask $0.25 \times \mathbf{1}_{2\times 2}$ to simulate sensor integration, and downsampled by a factor of two by discarding every other pixel in each direction. Zero mean Gaussian noise with different variances was then added to obtain a set of observed LR images. Panchromatic images were obtained from the original HR color images using the model in Equation (3), with $\lambda_b = 1/3$, for $b = 1, 2, 3$. The noise variances used in the experiments are summarized in Table 1.

We have used three different indices to measure the quality of the reconstructed images. Spatial improvement of reconstructed images has been assessed by means of the correlation of the high-frequency components (COR) [5] which measures the spatial similarity between each reconstructed multispectral image band and the panchromatic image. The COR index takes values between 0 and 1 (the higher the value the better the quality of the reconstruction). Spectral fidelity was assessed by means of the peak signal-to-noise ratio (PSNR) between each band of the reconstructed and original multispectral images, and the standard ERGAS index (from the French Erreur Relative Globale Adimensionalle de Synthése) [18], a dimensionless global criterion which considers the ratio of the root mean squared error and the bandwise mean. The lower the value of this index the higher the quality of the multispectral image.

In order to examine the behavior of the set of parameters $\bar{\alpha}_b$ and $\alpha_b(i, il)$ in Equations (20) and (25), respectively, we used different values for $\bar{\rho}_b$ and ρ_b [see Equations (28) and (29)] ranging from 0.25 to 6. We also used different values for $\bar{\mu}_b$ ranging from 0 to 1 and μ_b ranging from 0.9 to 1. Figure 3 plots the evolution, as a function of ρ_b and μ_b, of the mean PSNR, obtained by averaging the PSNR of all the bands of the multispectral image, for the reconstruction

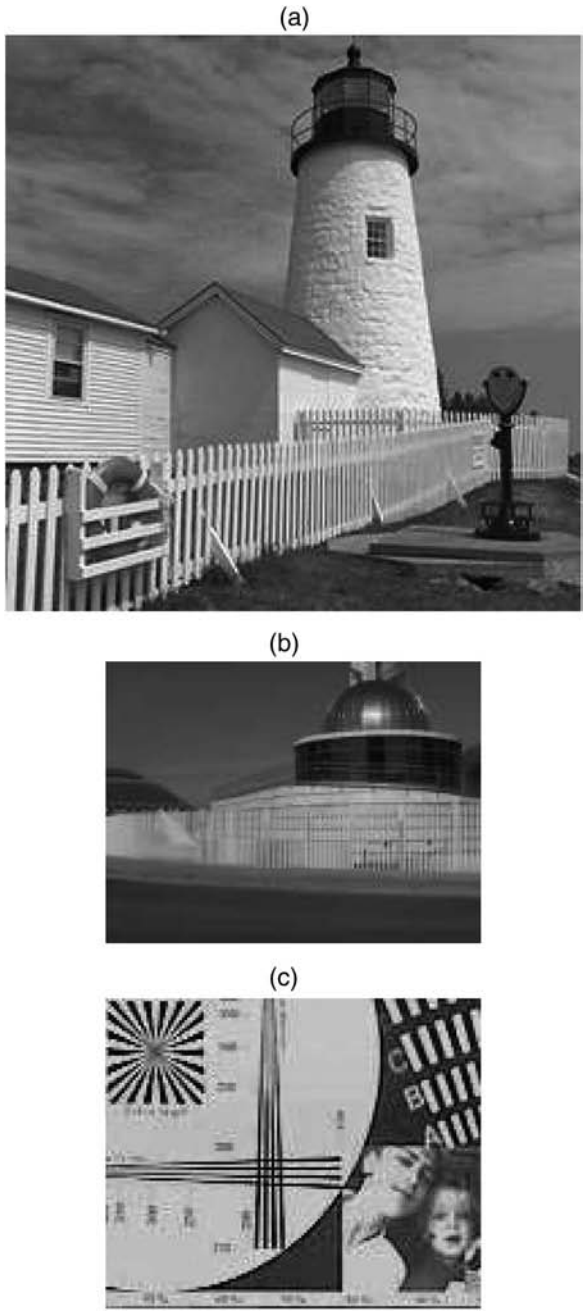

FIGURE 2. Color images used in the first experiment.

TABLE 1. Noise variances used for the multispectral and panchromatic images.

Type	Multispectral image noise variance, $\sigma^2_{n_b}$, for $b = 1, 2, 3$	Panchromatic image noise variance, σ^2_v
(i)	4	6.25
(ii)	16	25
(iii)	25	49
(iv)	49	100

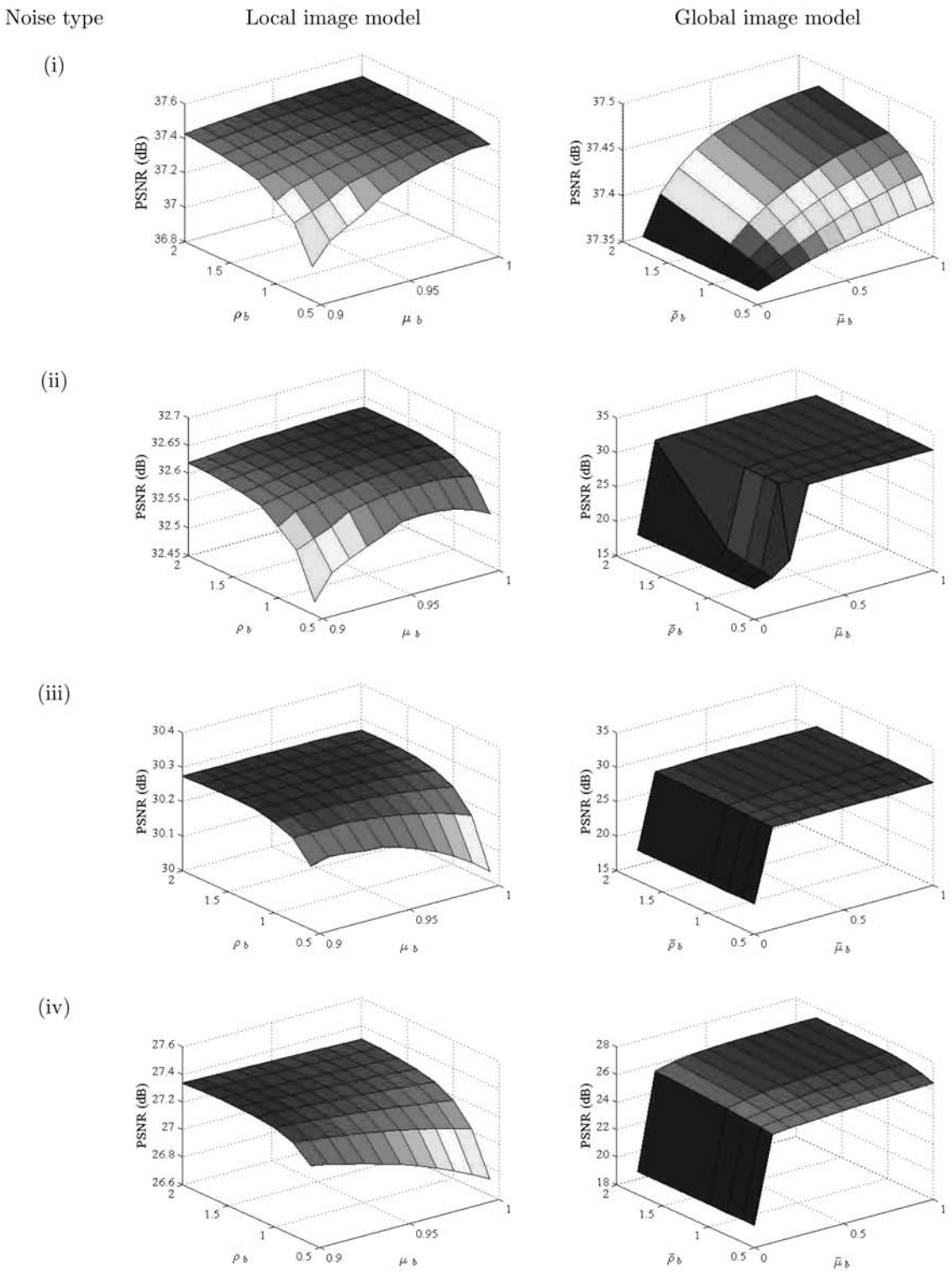

FIGURE 3. Mean PSNR evolution for the reconstruction of the image in Fig. 2c degraded with the noise variances described in Table 1.

of the image in Fig. 2c using a local image model for the different noise types in Table 1. Figure 3 also shows the mean PSNR evolution for the reconstruction using the global image model, as a function of $\bar{\rho}_b$ and $\bar{\mu}_b$. From Fig. 3, the similarity between the behavior of the global and local image models is remarkable. The higher the quality of the reconstructions the higher the values of ρ_b and $\bar{\rho}_b$, especially for lower noise cases.

Table 2 shows the values for the local model parameters ρ_b and μ_b, for $b = 1,2,3$, and the global model parameters, $\bar{\rho}_b$ and $\bar{\mu}_b$, corresponding to the best reconstructions in terms of PSNR for the images in Fig. 2 and the noise variances in Table 1. This table shows that, in general, the estimated value of the prior hyperparameter, α_b, is good enough to obtain good reconstructions, although, close to this value we can obtain slightly better reconstructions in terms of PSNR.

Tables 3–6 show the resulting PSNR, COR and ERGAS values for the reconstructions of the images in Fig. 2 for the noise configurations in Table 1. The results of bicubic interpolation and the pansharpening method in [6] have also been included for comparison. The reconstructed images corresponding to the figures of merit in Table 3 are displayed in Figs 4–6.

TABLE 2. Global and local image model parameter values resulting in the best reconstruction in terms of PSNR for the images in Fig. 2 and the noise variances in Table 1.

		Global model		Local model	
Noise	Image	$\bar{\rho}_b$	$\bar{\mu}_b$	ρ_b	μ_b
(i)	Figure 2a	0.5	1	0.5	1
	Figure 2b	1.8	0.9	0.8	0.92
	Figure 2c	5.6	1	2	1
(ii)	Figure 2a	1	1	1.2	0.98
	Figure 2b	1.8	0.9	1	0.9
	Figure 2c	1.8	1	1.6	0.98
(iii)	Figure 2a	1.8	0.9	1.2	0.91
	Figure 2b	1.8	0.6	0.8	0.9
	Figure 2c	1.8	1	1.6	0.92
(iv)	Figure 2a	1.8	0.9	1.2	0.9
	Figure 2b	0.8	0.9	0.6	0.9
	Figure 2c	3.2	0.6	1.4	0.9

For all images, the proposed local image model produces both numerically and visually better results. Note however that differences between the global and local image model are small when the parameters are chosen to produce the best PSNR value. This was expected since the information provided by the panchromatic image about image edges is very reliable, as we know exactly the degradation model in this simulation. Also, since the value of μ_b is very high for all the studied cases it does not allow for the local model to move too much away from the global model behavior. This is justified by the fact that, if μ_b is small, the local method allows for high variations in the values of $\alpha_b(i, il)$ and these produce images with hot and cold pixels, that is, isolated pixels that have values far away from the value of their neighbors. An example of such an effect is shown in Fig. 7 where $\mu_b = 0.1$ and $\rho_b = 1$ were used. Note the color differences on the edges of the fence and the isolated spots on the banister, for instance.

For all the studied cases, the bicubic interpolation produces over-smoothed reconstructions. The good performance of the method in [6] is noteworthy, which outperforms bicubic interpolation. As we will see later, this does not happen when dealing with real satellite images. This is probably justified by the degradation model used in [6], that adapts perfectly well to this reconstruction method. Note, however, that the method in [6] produces noisier reconstructions and some color bleeding at the edges, as can be observed in the center of the fence in Fig. 4d.

In a second experiment, the global and local image models are compared on real Landsat ETM+ images. Figure 8 depicts three 128×128 pixels false RGB color regions of interest composed of bands 3, 4 and 2 of a Landsat ETM+ multispectral image, together with their corresponding 256×256

TABLE 3. Values of PSNR, COR and ERGAS for the reconstructed color images in Fig. 2 with noise type (i).

		PSNR			COR			
Image	Band	1	2	3	1	2	3	ERGAS
Figure 2a	Bicubic interpolation	23.6	23.4	23.6	0.48	0.48	0.48	6.77
	Method in [6]	35.2	36.6	37.4	0.98	0.99	0.99	1.52
	Using the global image model	38	38.7	36.3	1	1	0.99	1.38
	Using the local image model	38	38.7	36.3	1	1	0.99	1.38
Figure 2b	Bicubic interpolation	29.2	29.2	29.2	0.53	0.55	0.55	4.55
	Method in [6]	37	38	38	0.95	0.97	0.97	1.73
	Using the global image model	38	38.3	38.1	0.98	0.99	0.98	1.61
	Using the local image model	38.6	38.8	38.5	0.99	0.99	0.99	1.53
Figure 2c	Bicubic interpolation	17.4	17.2	17.2	0.43	0.41	0.42	11.6
	Method in [6]	29.4	28.8	34	0.97	0.96	0.99	2.62
	Using the global image model	37.4	37.5	37.6	1	1	1	1.13
	Using the local image model	37.4	37.5	37.6	1	1	1	1.13

TABLE 4. Values of PSNR, COR and ERGAS for the reconstructed color images in Fig. 2 with noise type (ii).

		PSNR			COR			
Image	Band	1	2	3	1	2	3	ERGAS
Figure 2a	Bicubic interpolation	23.4	23.4	23.6	0.46	0.46	0.46	6.86
	Method in [6]	31.2	31.6	32	0.95	0.96	0.95	2.69
	Using the global image model	33.1	33	32.2	0.99	0.99	0.98	2.37
	Using the local image model	33	33.1	32.4	0.99	0.99	0.98	2.35
Figure 2b	Bicubic interpolation	28.8	28.8	28.8	0.49	0.50	0.51	4.78
	Method in [6]	32	32.4	32.2	0.87	0.90	0.89	3.21
	Using the global image model	33.4	33.4	33.2	0.96	0.96	0.95	2.81
	Using the local image model	33.7	33.5	33.5	0.95	0.94	0.94	2.73
Figure 2c	Bicubic interpolation	17.4	17.2	17.2	0.42	0.41	0.42	11.68
	Method in [6]	27.8	27.6	30.6	0.96	0.95	0.98	3.2
	Using the global image model	32.7	32.6	32.6	0.99	0.99	0.99	1.98
	Using the local image model	32.7	32.6	32.6	0.99	0.99	0.99	1.98

TABLE 5. Values of PSNR, COR and ERGAS for the reconstructed color images in Fig. 2 with noise type (iii).

		PSNR			COR			
Image	Band	1	2	3	1	2	3	ERGAS
Figure 2a	Bicubic interpolation	23.4	23.2	23.4	0.44	0.44	0.44	6.94
	Method in [6]	29	29.6	29.8	0.92	0.93	0.92	3.4
	Using the global image model	30.7	30.7	30.5	0.98	0.98	0.97	3.01
	Using the local image model	30.7	30.8	30.5	0.98	0.98	0.97	3.01
Figure 2b	Bicubic interpolation	28.4	28.4	28.4	0.44	0.46	0.46	4.93
	Method in [6]	30.2	30.2	30.2	0.80	0.84	0.83	4
	Using the global image model	31.4	31.4	31.4	0.92	0.91	0.91	3.51
	Using the local image model	31.7	31.7	31.7	0.89	0.89	0.89	3.39
Figure 2c	Bicubic interpolation	17.32	17.12	17.1	0.42	0.41	0.41	11.71
	Method in [6]	26.8	26.6	28.8	0.95	0.95	0.98	3.64
	Using the global image model	30.3	30.2	30.2	0.99	0.99	0.99	2.60
	Using the local image model	30.3	30.2	30.2	0.99	0.99	0.99	2.59

panchromatic images. The contribution of each multispectral image band to the panchromatic image, that is, the values of λ_b, $b = 1, 2, 3, 4$, was calculated from the spectral response of the ETM+ sensor. The obtained values were equal to 0.0078, 0.2420, 0.2239 and 0.5263, for bands one to four, respectively [12].

Note that, unlike the first experiment, in this one we do not have access to the true high-resolution images so numerical comparisons are not feasible.

In order to determine the value of the hyperparameters for the image model we proceed as follows. First, we simulate a 64×64 multispectral image and an 128×128 panchromatic image by convolving the observed multispectral and panchromatic images with the mask $0.25 \times \mathbf{1}_2 \times 2$ and downsampling them by a factor of two in each direction. Since multispectral images have different ranges depending on the band, to make them more similar, we normalized all the bands to have the same flux, that is, the same sum of the values in the band.

We, then, applied the reconstruction procedure described in the first experiment to these images to determine which combination of values of $\bar{\rho}_b$ and $\bar{\mu}_b$ and ρ_b and μ_b, (proportion and confidence parameters, respectively) for $b = 1, 2, 3, 4$, provides the best results. A summary of the obtained values is shown in Table 7. For reference, Table 8 depicts the resulting PSNR, COR and ERGAS values for the reconstruction of the simulated images with the different methods. We select the proportion and confidence parameters providing the best PSNR results.

We run the reconstruction procedure described in [12] on the observed low-resolution and panhcromatic images with

TABLE 6. Values of PSNR, COR and ERGAS for the reconstructed color images in Fig. 2 with noise type (iv).

		PSNR			COR			
Image	Band	1	2	3	1	2	3	ERGAS
Figure 2a	Bicubic interpolation	23.2	23	23.2	0.40	0.41	0.41	7.12
	Method in [6]	26.4	26.8	27.2	0.86	0.86	0.85	4.62
	Using the global image model	28.1	28.1	27.9	0.96	0.96	0.94	4.06
	Using the local image model	28.4	28.3	27.9	0.95	0.94	0.93	4
Figure 2b	Bicubic interpolation	27.8	27.8	27.8	0.37	0.38	0.40	5.34
	Method in [6]	27.4	27.4	27.2	0.69	0.71	0.73	5.59
	Using the global image model	29.5	29.5	29.5	0.80	0.80	0.78	4.38
	Using the local image model	29.9	29.8	29.8	0.78	0.78	0.77	4.21
Figure 2c	Bicubic interpolation	17.2	17	17	0.41	0.40	0.40	11.78
	Method in [6]	25	25	26.2	0.94	0.93	0.96	4.58
	Using the global image model	27.4	27.3	27.3	0.99	0.98	0.99	3.65
	Using the local image model	27.4	27.3	27.3	0.99	0.99	0.99	3.64

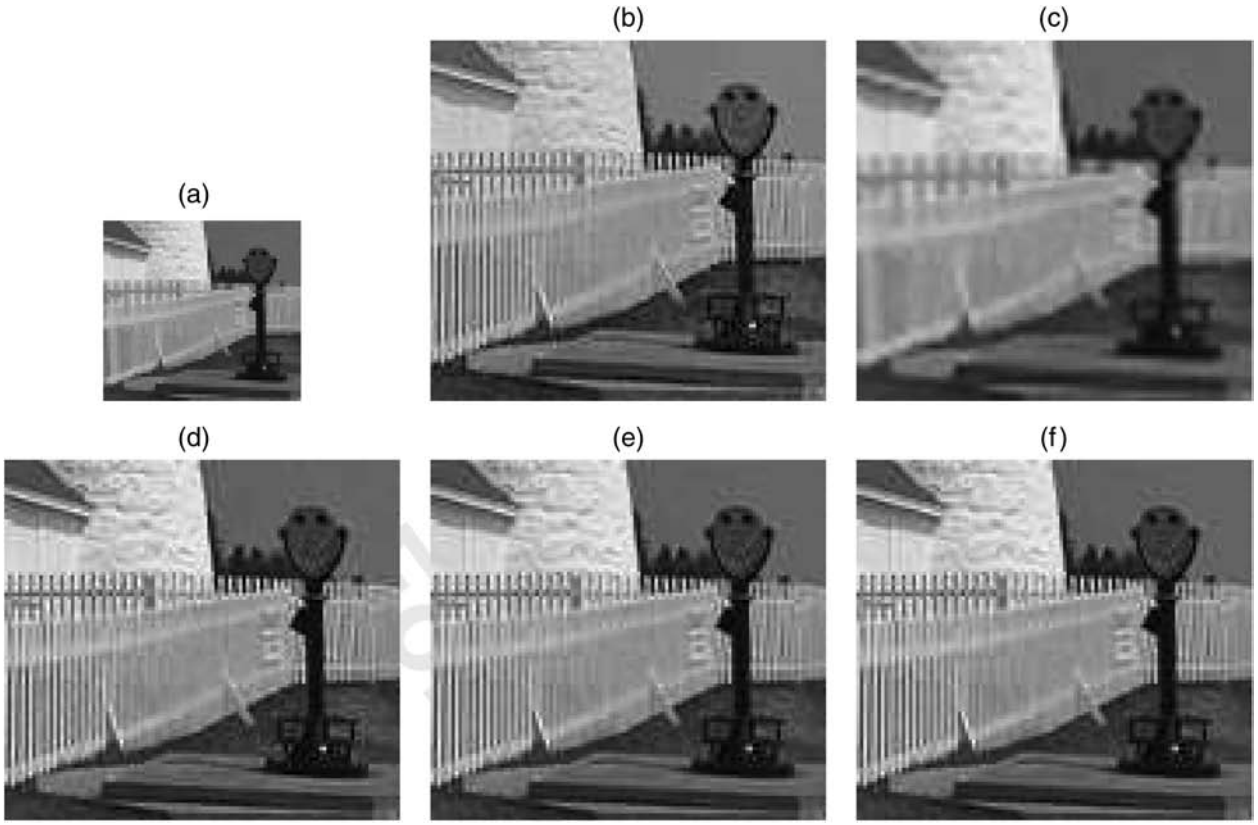

FIGURE 4. A detail of the image in Fig. 2a degrade with noise type (i): (a) observed multispectral image, (b) observed panchromatic image, (c) bicubic interpolation of (a), (d) reconstruction using the method in [6], (e) reconstruction using proposed the global image model, (f) reconstruction using the proposed local image model.

flat hyperpriors to obtain an estimate of the mean parameters γ, $\beta_1, \ldots, \beta_4$ and $\underline{\alpha}_1, \ldots, \underline{\alpha}_4$, for the observed 128×128 multispectral image.

Note that the rationale behind the approach used is that the proportion and confidence parameters will be roughly the same when a downsampling process is performed and again the observed low-resolution and panchromatic images with flat hyperpriors and a global image model are used to determine an initial mean value for the hyperparameters.

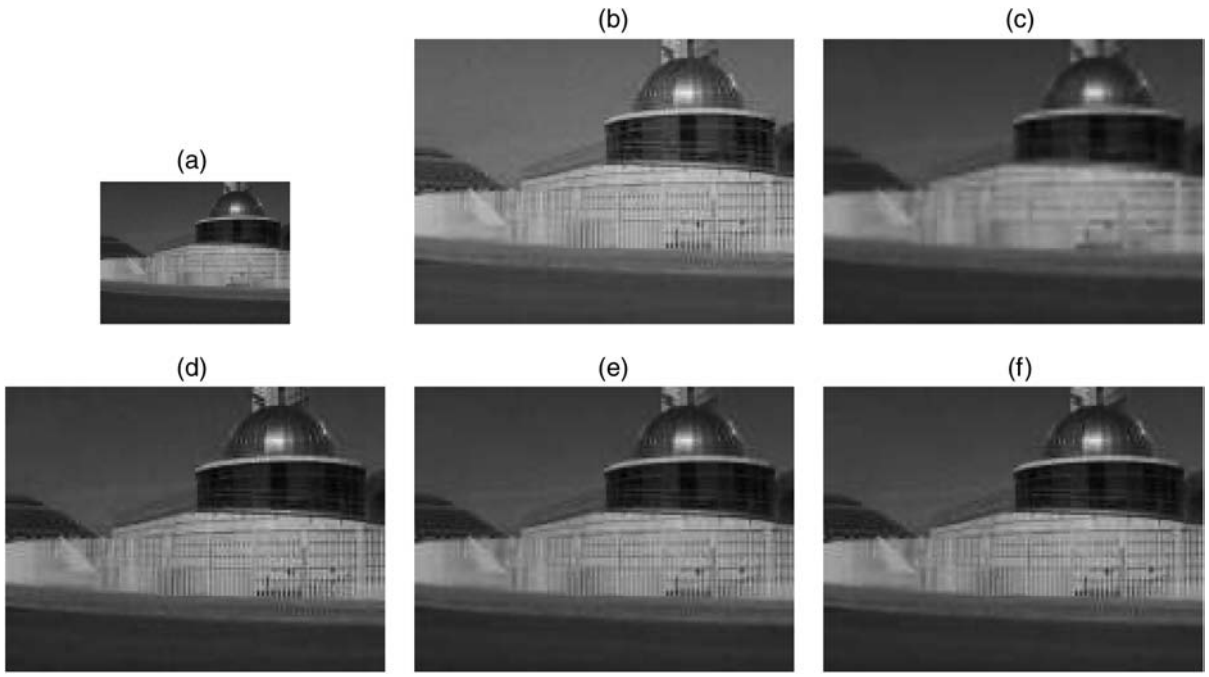

FIGURE 5. For the image in Fig. 2b degraded with noise type (i): (a) observed multispectral image, (b) observed panchromatic image, (c) bicubic interpolation of (a), (d) reconstruction using the method in [6], (e) reconstruction using the proposed global image model, (f) reconstruction using the proposed local image model.

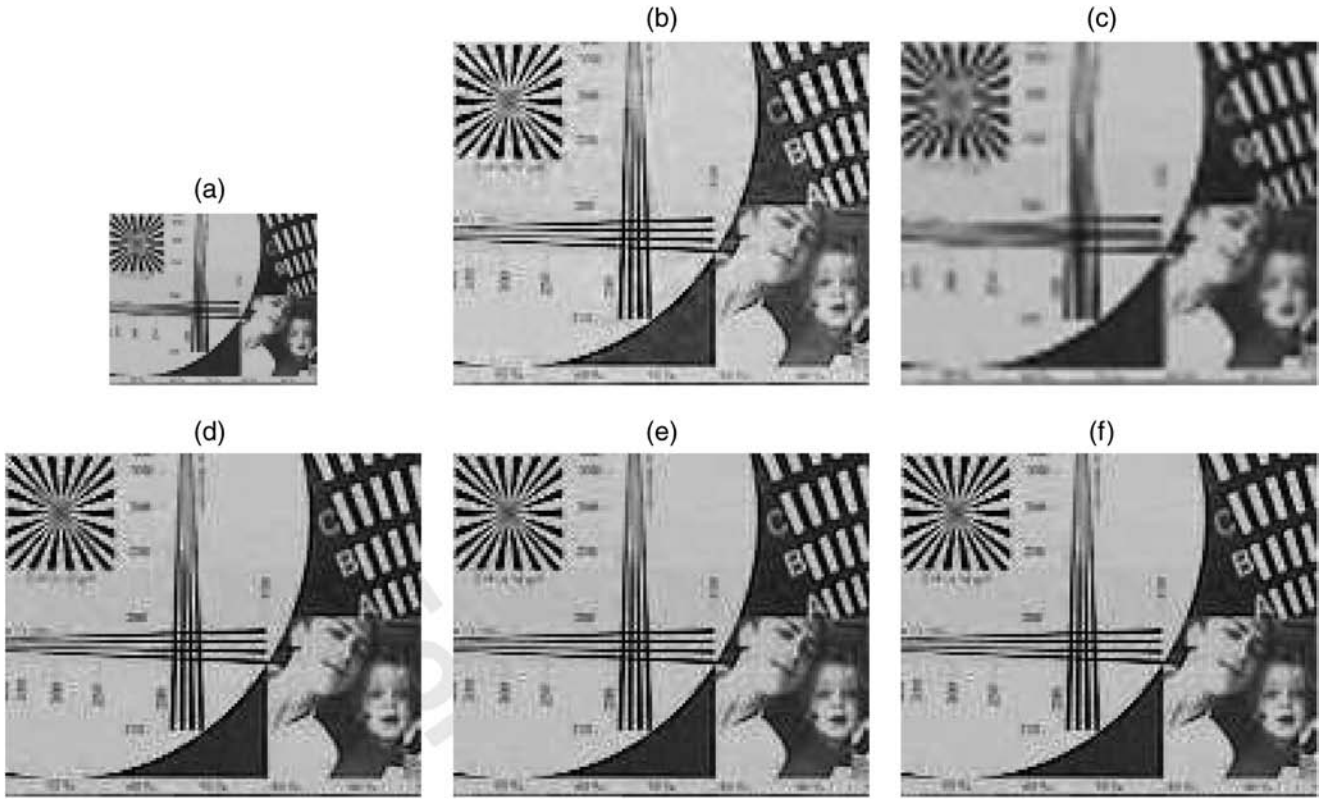

FIGURE 6. For the image in Fig. 2c degraded with noise type (i): (a) observed multispectral image, (b) observed panchromatic image, (c) bicubic interpolation of (a), (d) reconstruction using the method in [6], (e) reconstruction using the proposed global image model, (f) reconstruction using the proposed local image model.

Using the obtained mean values and the values of $\bar{\rho}_b$ and $\bar{\mu}_b$ and ρ_b and μ_b, $b = 1, 2, 3, 4$, previously determined, we reconstructed the observed 128×128 multispectral image using the proposed methods with the global and local image models. Figures 9 and 10 show the different reconstructions of the observed images in Figs. 8b and 8c, respectively.

Although the numerical results in Table 8 are referred to the low-resolution simulated images, looking at these figures of merit and the reconstructions in Figs 9 and 10, certain conclusions can be drawn.

Both proposed methods using the global and local image models provide better numerical and visual results than bicubic interpolation and the Price method in Ref. [6]. Bicubic interpolation results in oversmoothed reconstructions and with a low correlation of the high frequencies with the panchromatic image. The method in Ref. [6] produces crisp images but it introduces artifacts in the form of artificial blocks around borders (see, for instance, the harbor border in Fig. 9) and, although it obtains the highest mean COR value, it also introduces noise in the panchromatic image and, thus, results in lower PSNR values.

FIGURE 7. Reconstruction of the image in Fig. 2b degraded with noise type (i) using the proposed local image model, with $\mu_b = 0.1$ and $\rho_b = 1.0$ (note the isolated spots on the fence and banister and the strong color differences on the fence).

TABLE 7. Local model hyperparameter values giving the best reconstructions of multispectral images in Fig. 8.

		Global model		Local model	
Noise	Image	$\bar{\rho}_b$	$\bar{\mu}_b$	ρ_b	μ_b
a	1	0.25	1.0	0.25	0.91
	2	0.25	0.3	0.67	0.94
	3	0.25	0.4	0.67	0.90
	4	0.25	0.1	2.00	0.98
b	1	0.25	1.0	0.25	0.90
	2	0.25	1.0	0.33	0.96
	3	0.25	0.3	1.00	0.90
	4	0.25	0.2	2.00	0.98
c	1	0.25	1.0	0.25	0.90
	2	0.25	1.0	0.25	0.99
	3	0.25	1.0	0.67	0.90
	4	0.25	1.0	2.00	0.99

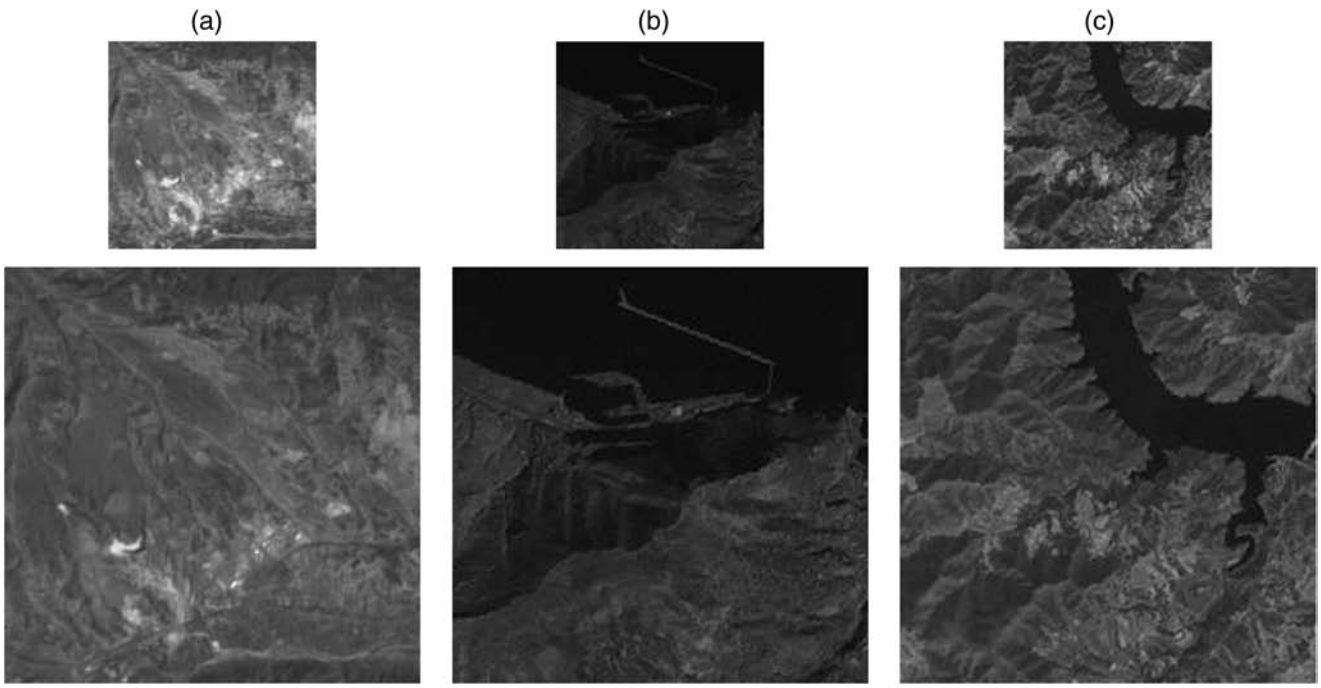

FIGURE 8. False RGB color images composed of the LR bands 3, 4 and 2 and panchromatic image, (a) observed in the region of Huercal-Overa (Spain), (b) observed in 2002/02/12 for Path/Row 198/35 and (c) observed in 2000/08/08 for Path/Row 199/031.

TABLE 8. PSNR, COR and ERGAS values for the Landsat ETM+ images reconstructions.

		PSNR				COR				
Image	Band	1	2	3	4	1	2	3	4	ERGAS
Figure 8a	Bicubic interpolation	32.29	30.72	28.44	35.36	0.58	0.59	0.59	0.59	3.05
	Method in [6]	31.14	29.56	27.23	34.10	0.84	0.87	0.86	0.86	3.50
	Using the global image model	32.06	31.40	29.03	35.77	0.58	0.75	0.75	0.83	2.91
	Using the local image model	32.42	31.80	29.49	35.77	0.58	0.81	0.81	0.90	2.80
Figure 8b	Bicubic interpolation	41.20	39.16	35.04	32.32	0.37	0.41	0.41	0.42	5.22
	Method in [6]	38.08	36.72	32.91	29.86	0.71	0.82	0.80	0.83	6.84
	Using the global image model	40.88	39.58	35.66	32.67	0.36	0.58	0.71	0.88	4.96
	Using the local image model	40.96	39.68	35.77	32.67	0.36	0.58	0.72	0.90	4.92
Figure 8c	Bicubic interpolation	33.37	30.80	26.65	32.12	0.46	0.48	0.49	0.49	5.04
	Method in [6]	31.66	29.46	25.51	30.79	0.86	0.91	0.91	0.91	5.83
	Using the global image model	33.40	31.62	27.84	33.66	0.45	0.67	0.79	0.90	4.46
	Using the local image model	33.40	32.18	28.31	33.66	0.45	0.75	0.86	0.95	4.41

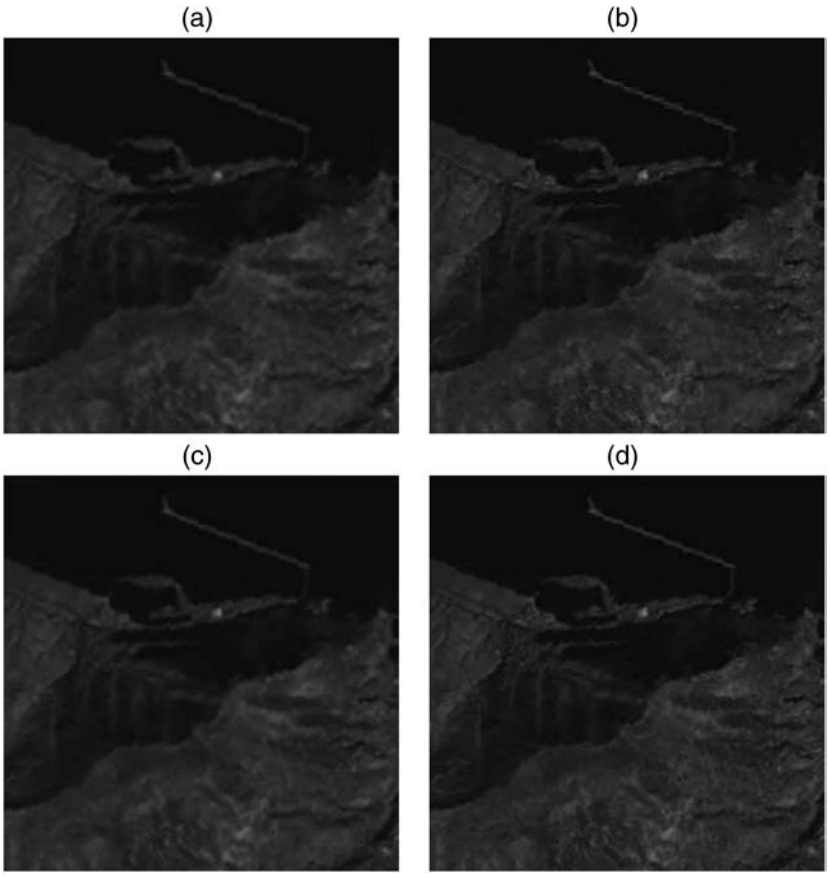

FIGURE 9. (a) Bicubic interpolation of the image in Fig. 8b, (b) reconstruction using the method in [6], (c) reconstruction using the global image model proposed, (d) reconstruction using the local image model.

The proposed method using the local image model provides the best numerical and visual results preserving the spectral properties of the multispectral image while successfully incorporating the high frequencies from the panchromatic image and controlling the noise in the image. For real multispectral images, the method using the local image model provides better reconstructions than the method using the global image model. This may be due to the fact that the modeling

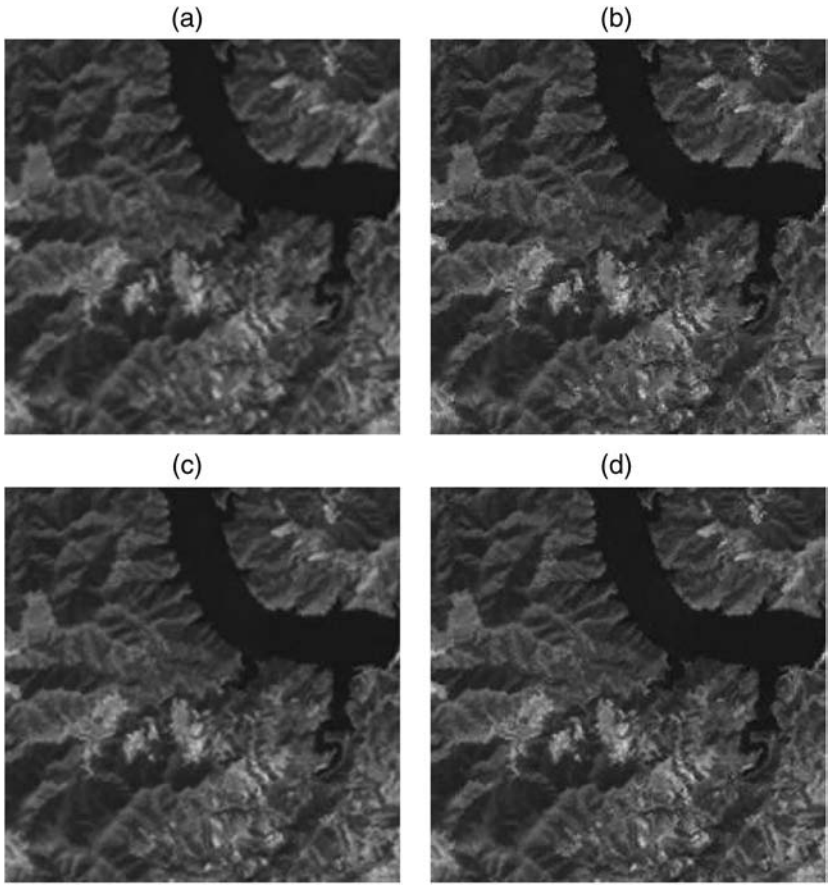

FIGURE 10. (a) Bicubic interpolation of the image in Fig. 8c, (b) reconstruction using the method in [6], (c) reconstruction using the global image model, (d) reconstruction using the local image model.

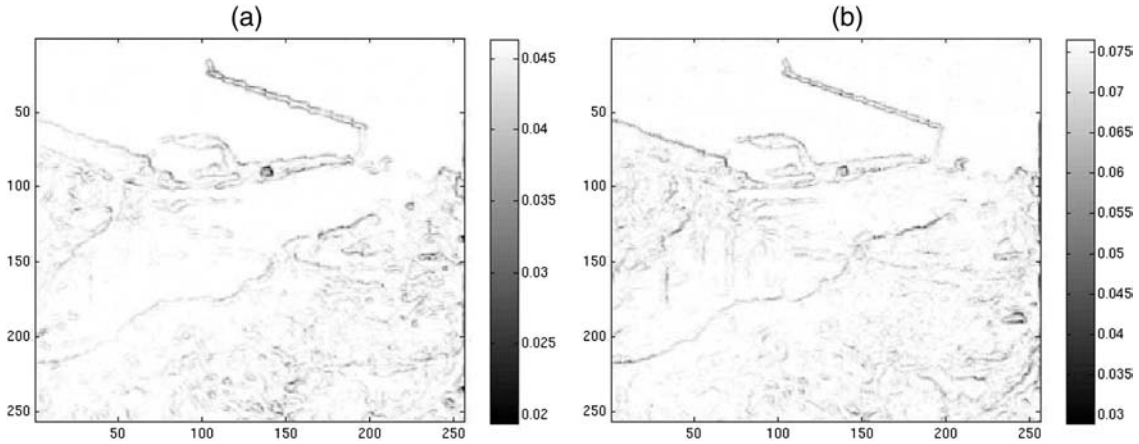

FIGURE 11. Plot of the values of (a) $\sum_{l=1}^{4} \alpha_3(i, il)$ and (b) $\sum_{l=1}^{4} \alpha_4(i, il)$, obtained for the reconstruction of the image in Fig. 8c, depicted in Fig. 9c.

of the degradation process is not very accurate, which consequently makes the prior model to play a stronger role in the reconstruction procedure. Note that the proposed method using the local image model results in higher PSNR and COR and a better ERGAS value than the other methods.

Both global and local methods are not very sensitive to variations on the value of λ_b if these values approximately reflect the contribution of each band to the panchromatic image. However, it seems that having bands with very different characteristics on range and flux makes the method in Ref.

[12] to underestimate the noise parameter of some bands and overestimate the noise parameter of the panchromatic image, leading to reconstructions where the information of the panchromatic image is mainly placed on one or two bands.

Figure 11 plots the values of $\sum_{l=1}^{4} \alpha_b(i, il)$ for bands 3 and 4 of the reconstruction in Fig. 10d, in which edges are clearly depicted corresponding to lower values of the regularization parameters.

We conclude this section by providing some information on the computing requirements of the algorithms. For our proposed method, the most demanding computational task, both in terms of processing and memory requirements, is the calculation of the reconstructed multispectral image. Each iteration of the algorithm using the global image model took 11.5 s to execute on a Xeon 3.2 GHz processor, for observed multispectral images of size 128×128, while each iteration of the algorithm using the local image model took 17.5 s. The algorithm using the global image model typically required 10 iterations to converge, while the algorithm using the local image model required about five iterations.

6. CONCLUSIONS

In this paper the reconstruction of multispectral images has been formulated from a super-resolution point of view. A hierarchical Bayesian framework has been presented to incorporate global and local prior knowledge on the expected characteristics of the multispectral images, model the observation process of both panchromatic and low-resolution multispectral images and also include information on the unknown parameters in the model in the form of hyperprior distributions. The proposed method has been tested experimentally on synthetic and real images, outperforming other widely used methods for solving the same problem.

FUNDING

This work has been partially supported by the Spanish research programme Consolider Ingenio 2010: MIPRCV (CSD2007-00018) and the Consejería de Innovación, Ciencia y Empresa of the Junta de Andalucía under contract P07-TIC-02698.

REFERENCES

[1] Program, N.L. Landsat ETM+ Scenes. *Global Land Cover Facility*. US Geological Surve, Sioux Falls, South Dakota. http://glcf.umiacs.umd.edu. Accessed on May 27, 2008.

[2] Carper, W.J., Lillesand, T.M. and Kiefer, R.W. (1990) The use of intensity-hue-saturation transformations for merging SPOT panchromatic and multispectral image data. *Photogramm Eng. Remote Sens.*, **56**, 459–467.

[3] Chavez, P.S., Sides, S. and Anderson, J. (1991) Comparison of three different methods to merge multiresolution and multispectral data: Landsat TM and SPOT panchromatic. *Photogramm Eng. Remote Sens.*, **57**, 295–303.

[4] Nuñez, J., Otazu, X., Fors, O., Prades, A., Pala, V. and Arbiol, R. (1999) Multiresolution-based image fusion with additive wavelet decomposition. *IEEE Trans Geosci. Remote Sens.*, **37**, 1204–1211.

[5] Vijayaraj, V. (2004) A quantitative analysis of pansharpened images. Master's Thesis, Mississippi St. University.

[6] Price, J. (1999) Combining multispectral data of different spatial resolution. *IEEE Trans. Geosci. Remote Sens.*, **37**, 1199–1203.

[7] Park, J. and Kang, M. (2004) Spatially adaptive multi-resolution multispectral image fusion. *Int. J. Remote Sens.*, **25**, 5491–5508.

[8] Eismann, M. and Hardie, R. (2005) Hyperspectral resolution enhancement using high-resolution multispectral imaginary with arbitrary response functions. *IEEE Trans. Geosci. Remote Sens.*, **43**, 455–465.

[9] Akgun, T., Altunbasak, Y. and Mersereau, R. (2005) Super-resolution reconstruction of hyperspectral images. *IEEE Trans. Image Process.*, **14**, 1860–1875.

[10] Molina, R., Katsaggelos, A.K. and Mateos, J. (1999) Bayesian and regularization methods for hyperparameter estimation in image restoration. *IEEE Trans. Image Process.*, **8**, 231–246.

[11] López, A., Molina, R., Katsaggelos, A.K. and Mateos, J. (2002) SPECT image reconstruction using compound models. *International Journal of Pattern Recognition and Artificial Intelligence*, **16**, 317–330.

[12] Molina, R., Vega, M., Mateos, J. and Katsaggelos, A. (2008) Variational posterior distribution approximation in Bayesian super resolution reconstruction of multi-spectral images. *Applied and Computational Harmonic Analysis*, **24**, 251–267.

[13] Chandas, J., Galatsanos, N.P. and Likas, A. (2006) Bayesian restoration using a new hierarchical directional continuous edge image prior. *IEEE Trans. Image Process.*, **15**, 2987–2997.

[14] Molina, R., Mateos, J. and Katsaggelos, A. (2007) Super Resolution of Multispectral Images Using Locally Adaptive Models. *2007 European Sig. Proc. Conf. (EUSIPCO 2007)*, Vol. 9, pp. 1497–1501.

[15] Berger, J.O. (1985) *Statistical Decision Theory and Bayesian Analysis*. Springer, New York.

[16] Kullback, S. and Leibler, R.A. (1951) On information and sufficiency. *Ann. Math. Stat.*, **22**, 79–86.

[17] Kullback, S. (1959) *Information Theory and Statistics*. Dover Publications, Mineola, NY.

[18] Wald, L., Ranchin, T. and Mangolini, M. (1997) Fusion of satellite images of different spatial resolutions: assessing the quality of resulting images. *Photogramm. Eng. Remote Sens.*, **63**, 691–699.